Computational and Structural Biotechnology Journal 19 (2021) 5600–5612

COMPUTATIONAL AND STRUCTURAL BIOTECHNOLOGY JOURNAL

journal homepage: www.elsevier.com/locate/csbj

Structural determinants of ligands recognition by the human mitochondrial basic amino acids transporter SLC25A29. Insights from molecular dynamics simulations of the c-state

Andrea Pasquadibisceglie [a], Fabio Polticelli [a,b,*]

[a] Department of Sciences, Roma Tre University, 00146 Rome, Italy
[b] National Institute of Nuclear Physics, Roma Tre Section, 00146 Rome, Italy

ARTICLE INFO

Article history:
Received 28 May 2021
Received in revised form 16 September 2021
Accepted 4 October 2021
Available online 7 October 2021

Keywords:
Mitochondrial carrier of basic amino acids
SLC25A29
Ligand recognition
Molecular docking
Molecular dynamics

ABSTRACT

In mitochondria, metabolic processes require the trafficking of solutes and organic molecules, such as amino acids. This task is accomplished by the Mitochondrial Carrier Family members (also known as SLC25), among which the SLC25A29 is responsible for the translocation of basic amino acids. In this regard, nitric oxide levels originated by the arginine mitochondrial catabolism have been shown to strongly affect cancer cells' metabolic status. Furthermore, the metabolic disease saccharopinuria has been linked to a mitochondrial dysregulation caused by a toxic intermediate of the lysine catabolism. In both cases, a reduction of the activity of SLC25A29 has been shown to ameliorate these pathological conditions. However, no detailed structural data are available on SLC25A29. In the present work, molecular modelling, docking and dynamics simulations have been employed to analyse the structural determinants of ligands recognition by SLC25A29 in the c-state. Results confirm and reinforce earlier predictions that Asn73, Arg160 and Glu161, and Arg257 represent the ligand contact points I, II, and III, respectively, and that Arg160, Trp204 and Arg257 form a stable interaction, likely critical for ligand binding and translocation. These results are discussed in view of the experimental data available for SLC25A29 and other homologous carriers of the same family.

1. Introduction

The Mitochondrial Carrier Family (MCF), also known as Solute Carrier Family 25 (SLC25), is involved in the translocation of a wide range of molecules across the inner mitochondrial membrane (IMM). The SLC25 family members are characterized by three homologous domains consisting of two long transmembrane α-helices connected by a shorter one. This symmetry is reflected also by the presence of a conserved motif signature PX[DE]XX[KR], repeated in all the three domains. The charged residues of this motif form a salt bridges network on the matrix side of the carrier, when this is open towards the intermembrane space (IMS) (*i.e.*, in the cytoplasmic state or c-state). A second less conserved motif is [FY][DE]XX[KR], which is involved in another salt bridges network that closes the IMS side of the transporter when the matrix side is open (*i.e.*, the matrix state or m-state). The crystal structure of the bovine ADP/ATP transporter (bANT1) in the c-state [1] and the recently solved structure of ANT1 from *Thermothelomyces thermophila* in the m-state [2] helped to clarify numerous aspects of the SLC25 family carriers structure. In particular, it has been observed that Tyr and Gln residues are involved in the stabilization of the cytoplasmic and matrix networks, respectively. Moreover, the closure of the cytoplasmic side is also assured by several hydrophobic residues forming a cytoplasmic plug and by the presence of Gly and other residues with small side chains on the α-helices interfaces [2,3].

Comparative modelling and analyses of asymmetrically conserved residues allowed to propose a common binding site hypothesis [4,5]. In particular, for each class of ligands three binding residues (*i.e.*, contact points, CPs) with a defined role have been identified. The first CP was proposed to discriminate between different ligands of the same class; for instance, Asp or Glu residues, in basic amino acids carriers, should be frequently conserved as CP I, being likely involved in the recognition of the positively charged side chain of the ligand. On the other hand, CP II has been suggested to have a role in the discrimination of different ligand

* Corresponding author at: Department of Sciences, Roma Tre University, Viale Guglielmo Marconi 446, 00146 Rome, Italy.
E-mail address: fabio.polticelli@uniroma3.it (F. Polticelli).

https://doi.org/10.1016/j.csbj.2021.10.007

classes (*i.e.*, R[DE] for amino acids transporters); and CP III, usually made up by Arg or Lys residues, has been proposed to stabilize interaction with the ligand.

SLC25A29 is a member of the MCF and it is mainly involved in importing basic amino acids into the mitochondrial matrix, with a preference for arginine and lysine [6]. Initially, this protein was identified as a carnitine/acylcarnitine transporter [7] and then, given its ability to rescue the deficient ornithine metabolism in patients affected by hyperornithinemia-hyperammonemia-homocitrullinuria syndrome, it has been suggested to be an ornithine transporter [8]. Only recently, a study conducted by Palmieri and coworkers demonstrated that SLC25A29 is mainly involved in the translocation of basic amino acids [6]. Noteworthy, in 2018 a study linking the overexpression of this carrier to the cancer cells' metabolic status was published [9]. In particular, knocking-out SLC25A29 in cancer cells significantly reduced their proliferation rate, both *in vitro* and *in vivo*, affecting the mitochondria-derived nitric oxide (NO) levels, enhancing mitochondrial respiration, and reducing glycolysis. At the same time, depletion of SLC25A29 in animal models for saccharopinuria strongly decreased the levels of saccharopine, a toxic intermediate of the lysine catabolism [10].

Given the potential biomedical interest of this protein, and following several computational studies on ANT1 [11–17], in the present work an *in silico* characterization of the structure and mechanism of SLC25A29 has been carried out. The analyses were specifically focused on the mechanism of recognition of the arginine and lysine ligands, aiming at identifying critical residues in ligand binding and translocation.

2. Methods

2.1. Sequence analyses

The canonical human SLC25A29 protein sequence (UniProt ID: Q8N8R3-1) has been used to produce a pairwise sequence alignment with the bovine SLC25A4 mature sequence (bANT1; UniProt ID: P02722-1). The alignment has been built using HHpred web server (https://toolkit.tuebingen.mpg.de/tools/hhpred) [18]. Conserved motives and contact points have been identified based on the multiple sequence alignment reported in the study by Ruprecht and coworkers [2]. Disordered regions have been detected using the webserver IUPred2A (https://iupred2a.elte.hu/) [19].

2.2. Molecular dynamics simulations

Given the high structural conservation among the SLC25 family members, the human SLC25A29 protein structure has been built by homology using MODELLER [20] and the bANT1 three-dimensional structure as template (PDB ID: 1OKC) [1]. This template has been chosen because the corresponding protein displays the highest sequence similarity with SLC25A29 and the 1OKC structure is the one with the best resolution (2.2 Å). The quality of the model was assessed through MolProbity (Table S1) [21]. The c-state conformation was verified measuring the pore dimension using HOLE2, implemented in MDAnalysis (Fig. S1) [22,23]. The transporter has been inserted in a lipid bilayer mimicking the mitochondrial inner membrane [24,25], using the web server CHARMM-GUI (http://www.charmm-gui.org/) [26]. Each layer of the lipid membrane is composed of 56 phosphatidylcholine (POPC), 44 phosphatidylethanolamine (POPE) and 25 double-negatively charged tetraoleyl cardiolipin (TOCL2) molecules. The water thickness chosen for the top and bottom sides of the system is 25 Å, using a TIP3P water model. Na^+ ions were added to neutralize the total system charge, while an excess of NaCl ions was added to reach the physiological concentration of 0.15 M (for system details see Table S2). The CHARMM36m force field [27] and AMBER 18 package have been used for all the MD simulations [28]. The system has been first energy minimized with 5000 steps of steepest descent and 5000 steps of conjugate gradient, applying positional restraints on the protein residues. Simulations have been carried out using periodic boundary conditions. For the long range non-bonded interactions, the Particle Mesh Ewald method and a 10 Å cut-off has been used [29]. A first thermalization phase from 0 to 100 K and a second slow phase from 100 to 310 K have been performed, using the NVT ensemble for a total of 600 ps. Lipid and protein atoms were restrained using a force constant of 10 kcal mol^{-1} $Å^{-2}$. The system was equilibrated in the NPT ensemble, in 10 different steps of 500 ps each, applying a 1 kcal mol^{-1} $Å^{-2}$ force constant on the protein atoms and constant pressure of 1 bar (~0.987 atm). Before the production phase, a last equilibration step has been performed without restraints, to relax the system. Finally, a 200 ns of conventional MD simulations have been performed in the NPT ensemble. The Langevin thermostat has been used for both NVT and NPT ensembles [30], while for the pressure control the Berendsen barostat with a semiisotropic pressure scaling has been used [31]. The covalent bonds involving hydrogen atoms have been restrained with the SHAKE algorithm [32]. The thermodynamic equilibrium of the system was verified analysing the time evolution of system density, kinetic, potential and total energy (Figs. S2, S3). The stability of the lipid bilayer has been assessed performing area per lipid, thickness, mass density and order parameters analyses (Figs. S4–S9).

2.3. Ensemble docking

GROMACS 2019.2 package [33] was used to perform a clustering of the MD trajectory, using the gromos algorithm [34]. This was performed taking into account the RMSD value of the backbone atoms of the first 282 protein residues (excluding the C-terminal tail) (Fig. S10) and using a 1 Å RMSD cut-off. From this procedure, the centroids of the first ten clusters have been extracted and used for the molecular docking simulations with the arginine and lysine ligands (ARG and LYS). It must be noted that these first ten clusters are composed only by frames deriving from the part of the trajectory where the RMSD value is at equilibrium. Receptor and ligand have been converted to pdbqt format using the MGLTools scripts "*prepare_receptor4.py*" and "*prepare_ligand4.py*" [35]. The docking simulations have been performed using AutoDock Vina [36]. Then, the resulting ARG and LYS docking poses have been clustered with the same approach described above, calculating the RMSD without a previous fitting and imposing a 4.2 Å cut-off value. Subsequently, the centroids of the first five clusters have been extracted. The system containing the protein–ligand complex, corresponding to each centroid, has been rebuilt with CHARMM-GUI [26] and used for 200 ns MD simulations trajectories (named MD1, MD2, MD3, MD4 and MD5), following the same procedures described in Section 2.2.

2.4. Simulations analyses

MD trajectories have been analysed using GROMACS 2019.2 and CPPTRAJ packages [33,37]. RMSD and RMSF analyses have been performed considering only the backbone atoms of the first 282 protein residues (excluding the C-terminal tail) (Figs. S10–S15). Time evolution of the radius of gyration of the α-carbons of the cytoplasmic/matrix network residues has been also analysed (Figs. S16, S17). For the hydrogen bonds and salt bridges analyses, given the high number of interactions observed, only the interactions with a persistence higher than 20% of the simulation time have been reported to limit the description to the most relevant

ones. The salt bridges analysis has been performed through the *hbond* command of CPPTRAJ package, considering only the charged residues, imposing a cut-off distance of 4 Å and removing the angle cut-off. For the cation-π analysis, the angles have been calculated taking the dot product between the normal vector to Trp204 aromatic ring plane and the normal vectors to the Arg257 and Arg160 guanidinium group planes, respectively. This has been carried out using the *vector* and *vectormath* commands of CPPTRAJ package. MDAnalysis [23] has been used for the bilayer membrane thickness analyses, while FATSLiM [38] has been used for the area per lipid calculation. Finally, raw data have been parsed and plotted using pandas, Matplotlib and Seaborn Python libraries [39,40]. Protein/ligand figures have been produced using UCSF Chimera 1.14 [41].

3. Results

3.1. Sequence analyses

The mitochondrial carrier SLC25A29 is formed by three homologous sequence repeats, each of which consists of two transmembrane α-helices and one loop containing a shorter matrix α-helix, likewise other SLC25 family members [42]. In particular, H1-h12-H2 helices form domain 1, whereas H3-h34-H4 and H5-h56-H6 form domain 2 and 3.

Analysis of the sequence alignment between the SLC25A29 and the bovine SLC25A4 (bANT1; PDB ID: 1OKC) [1], the well-characterized member of the SLC25 family, reveals that: the GXXXG/πXXXπ motives (orange/yellow circles, Fig. 1), the Gln braces (Gln30,Gln121,Gln218; green squares, Fig. 1), the three matrix network motives (red boxes, Fig. 1), the cytoplasmic gate (orange boxes, Fig. 1) and one Tyr brace (Tyr172) are conserved, while the cytoplasmic motives and two Tyr braces (Gln80 and Val269) are not (blue boxes and cyan squares, Fig. 1) [2]. In particular, the charged residues of the cytoplasmic network are replaced by uncharged amino acids (*i.e.*, Gly81, Leu84, Thr176, Thr270, Leu273). Obviously, the residues forming the three contact points (CPs) cannot be conserved with respect to bANT1, considering the different nature of the transported solutes. However, comparison of the two sequences allows to predict that the CPs for SLC25A29 should be Gly68 (CP I), Arg160/Glu161 (CP II) and Arg257 (CP III).

Interestingly, a unique feature of this protein is the long C-terminal tail (from Pro283 to Leu303). This is not conserved in other mitochondrial transporters, and the webserver IUPred2A (https://iupred2a.elte.hu/) [19] predicts this region to be disordered.

3.2. Ligands recognition

A three-dimensional structural model of the c-state protein conformation has been built by homology, using the bANT1 crystal structure (PDB ID: 1OKC) as template ([1]; see Methods for details). The model statistics calculated using MolProbity [21] (Table S1) indicate that the model has a good quality, in particular for what concerns the model structures used to perform the MD simulations with the ligands (see below). The SLC25A29 structure has been inserted in a lipid bilayer membrane and solvated, using the web-server CHARMM-GUI (Table S2) [26]. The system has been simulated using unbiased molecular dynamics (MD0) for a total of 200 ns. The centroids of the first 10 clusters have been used to perform an ensemble docking procedure. The resulting docking poses have been in turn clustered obtaining five complexes for each ligand (ARG or LYS; for details see Methods section). The initial structures have been compared with each other showing significantly different RMSD values, except for MD1-ARG and MD3-ARG, in which, although starting from the same protein conformation, two different docking poses and different interactions were obtained (Tables 1, 2). The ten final complexes obtained have been simulated for additional 200 ns each, generating 5 trajectories for both ARG and LYS (named MD1, MD2, MD3, MD4, MD5) for a total of 1 μs for each ligand. This has been done to verify the reliability of the docking poses and to analyse the behaviour of the ligands inside the transporter.

For both ligands, only three MD simulations have been considered for further analyses, because, in two of those, both ARG and LYS came out of the protein.

These six MD simulations have been analysed to identify and describe critical protein–ligand, intraprotein and protein-lipid interactions.

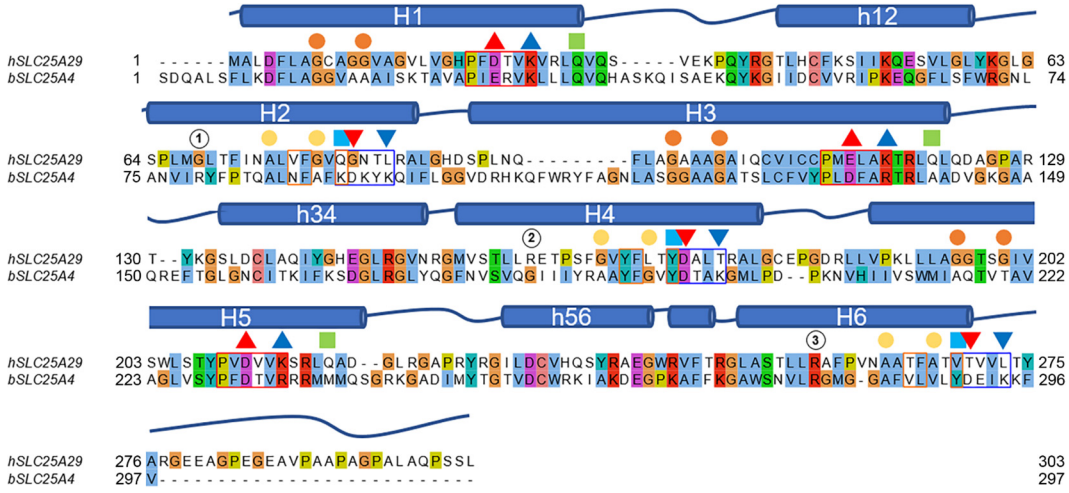

Fig. 1. Sequence alignment between human SLC25A29 and bovine SLC25A4. The secondary structure elements are depicted on top of the alignment (loops as lines and helices as cylinders). The cytoplasmic and matrix network motives are evidenced by blue and red boxes, and the corresponding charged residues with down and up triangles, respectively (blue for positively charged and red for negatively charged). The hydrophobic plug residues are indicated by orange boxes. The glutamine braces (Q braces) and tyrosine braces (Y braces) are identified with green and cyan squares. Orange and yellow circles indicate the GxxxG and πxxxπ motifs. The three contact points are highlighted by open circles with the corresponding number. The alignment has been visualized with Jalview [43] using the Clustal color scheme. (For interpretation of the references to color in this figure legend, the reader is referred to the web version of this article.)

Table 1
RMSD values (Å) calculated from the comparison between the coordinates of the three starting poses for each ligand.

	ARG		
	MD1	**MD3**	**MD4**
MD1	0	5.50	17.27
MD3	5.50	0	18.12
MD4	17.27	18.12	0
	LYS		
	MD1	**MD3**	**MD4**
MD1	0	4.63	6.5
MD3	4.63	0	7.34
MD4	6.50	7.34	0

3.2.1. Arginine interactions

During MD1, ARG established strong hydrogen bonds and salt bridges with residues of the matrix network (*i.e.*, Asp23, Lys26, Glu114 and Asp211) (Tables S3, S4, Fig. 2). However, the ligand resulted also stably bound to Thr254 for more than 80% of the simulation time (Table S3, Figs. 2, 3). The distances between ARG and the above-mentioned residues were stable and lower than 5 Å (apart from a short fluctuation of the ARG-Thr254 distance) (Fig. S18). Moreover, several water-mediated hydrogen bonds also occurred, including one connecting Asp23 to ARG (Table 3). Also several hydrophobic interactions were established by the aliphatic chain of ARG, of which the most significant were formed with Trp204, Tyr208 and to a lower extent with Leu69 (Fig. 3; Table S5).

During the MD3 trajectory, ARG moved from the initial docking pose, located near the matrix network, toward the centre of the transporter. Here, several hydrogen bonds and salt bridges were established between the carboxyl group of the ligand and the guanidinium group of Arg257, and between the α-amino group of ARG and the carboxyl group of Glu161. Of note, the ARG-Arg257 interaction was observed for more than 90% of the simulation time (Fig. 3, Fig. 4, Tables S3, S4). The ligand was also involved in two water-mediated hydrogen bonds: one with Arg160 (∼30% of the trajectory), and one with Glu114 (20% of the trajectory) (Table 3; Fig. S19).

The distance ARG-Arg257 was on average 3.4 Å, whereas that from Glu161 and Arg160 was ∼10 Å during the first 40 ns, while decreased for the subsequent 160 ns to 4 Å and 5 Å, respectively (Fig. 4). Contacts analysis revealed also that the ligand established hydrophobic interactions with several apolar residues, and in particular with Val16, Leu69, Trp204 and Val261 (Fig. 3, Table S5).

As in MD3, during the MD4 trajectory the carboxyl group and the guanidinium group of ARG formed hydrogen bonds and salt bridges with Arg257 and Glu161, respectively. The interactions with Arg257 were present for nearly all of the trajectory (∼90%), while the hydrogen bonds established with Glu161 were present for a fraction of frames equal to a maximum of 65% (Tables S3, S4). A weak hydrogen bond occurred between the ARG α-amino group and the side chain oxygen of Gln106, although with a maximum persistence of only 20% (Table S3). Similar to MD3, the distances from Arg257 and Arg160 were on average 3.4 Å and (after 80 ns) 4.8 Å, while the distance from Glu161 was approximately 3.3 Å (Fig. 4). Furthermore, the ligand established four water-mediated hydrogen bonds, of which that with Arg160 and that with Asn73 were present for 40% and 35% of the trajectory, respectively (Table 3; Fig. S19).

Finally, the aliphatic chain of ARG was also in contact with several hydrophobic residues, in particular with Val16, Leu69, Phe165, Trp204 and Val261 (Fig. 3, Table S5).

3.2.2. Lysine interactions

To further validate the data obtained from the SLC25A29-ARG MD simulations, simulations in presence of LYS ligand have been carried out as well.

As mentioned before, also in the case of LYS, the ligand reached a stable binding mode in three out of the five MD trajectories.

During the first of the three simulations, LYS established strong hydrogen bonds and electrostatic interactions with Glu114 and Lys117 for the first part of the trajectory, while in the second part it moved towards the central binding site interacting with Arg257 and Glu161 (Tables S6 and S7). Also a water-mediated hydrogen bond was established with Asp23 for almost 30% of the trajectory (Table 3). Moreover, the main hydrophobic interactions were established with Val16, Leu69 and Trp204, and the large part of these interactions were established during the second half of the trajectory (Fig. 5, Table S8).

In MD3, the ligand LYS initially interacted with Lys26, interaction later replaced by weaker electrostatic interactions with Arg257 (Fig. 5, Tables S6 and S7). On the contrary, the α-amino group and the side chain amino group both interacted for almost the entire trajectory with Glu114 and Glu161, respectively, with the latter being the most stable interaction (Fig. 5, Tables S6 and S7). Among the hydrophobic contacts, the most significant were with Val16, Trp204 and Val261 (Table S8). No significant solvent mediated interactions were established.

During the MD4 simulation, LYS was steadily bound to Glu114, Lys117 and Glu161 (Fig. 5, Tables S6 and S7). A water-mediated hydrogen bond between the ligand and Asp23 was present with a persistence of 90% (Table 3). Lastly, several hydrophobic interactions were established of which the most significant were those with Val16, Leu69, and Trp204 (Fig. 5, Table S8).

3.3. Intradomain and interdomain interactions

The intraprotein interactions were analysed in all the six MD simulations, in which one of the ligands was present, and compared with the MD0 (Fig. 6, Tables S9–S12, Fig. S20).

The SLC25 transporters are characterized by a particular type of interdomain interactions called: cytoplasmic and matrix network. In the case of the SLC25A29, only the matrix network charged residues result to be conserved, as also suggested by the electrostatic interaction analysis (Fig. 6, Tables S9 and S10). The interaction Asp23-Arg257 resulted to be one of the longest lasting in all the trajectories. Asp211 interacted with Lys26 for most of the simulations, although in MD3 and MD4, when the ligand ARG was present, it interacted with Arg160 for a longer fraction of time.

Table 2
RMSD values (Å) calculated from the comparison between the coordinates of all the protein conformations.

	MD1-ARG	**MD3-ARG**	**MD4-ARG**	**MD1-LYS**	**MD3-LYS**	**MD4-LYS**
MD1-ARG	0	0	1.69	2.76	2.52	2.02
MD3-ARG	0	0	1.69	2.76	2.52	2.02
MD4-ARG	1.69	1.69	0	3.07	2.62	2.19
MD1-LYS	2.76	2.76	3.07	0	1.09	1.61
MD3-LYS	2.52	2.52	2.62	1.09	0	1.38
MD4-LYS	2.02	2.02	2.19	1.61	1.38	0

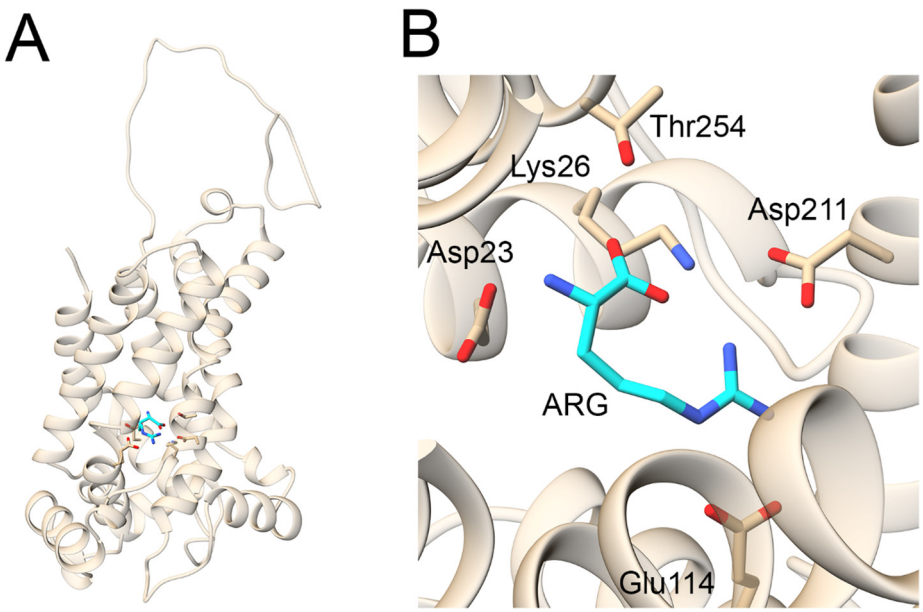

Fig. 2. ARG recognition mode during the first molecular dynamics simulation (MD1). Representative snapshot of the MD1 simulation of the ARG-SLC25A29 complex (side-view, A; top-view, B). Protein residues involved in electrostatic interactions with the ligand are shown in stick representation and coloured in tan, while ARG is coloured in cyan. (For interpretation of the references to color in this figure legend, the reader is referred to the web version of this article.)

Interestingly, the salt bridge between Glu114 and Lys214 was observed in all the simulations, except for the MD1-ARG and MD3-LYS simulations. Furthermore, during MD3 this interaction was established just for a small fraction of the time (36%). In this regard, the distances between the side chains of the matrix network residues have been analysed (Fig. 6).

As also evident from the results of the salt bridge and hydrogen bond analyses, Asp211-Lys26 and Glu114-Lys214 represent the main interacting couples of the matrix network. However, the presence of the ligands appears to perturbate these interactions, in particular ARG during MD3 and MD4 (Fig. 6). The H1 residue Asp23 resulted to establish the most stable interaction with Arg257, while it did not interact with the H3 charged residue Lys117, at variance with what observed for orthologous residues in the bANT1 crystal structure, but in agreement with results obtained by MD simulations of this latter transporter (see Discussion) [16].

Several electrostatic interactions were found between the loops and α-helices residues on the matrix side of the transporter (Tables S9 and S10). In detail, the most frequent intradomain interactions were: Asp220-Arg227, Glu53-Lys60, Glu242-Arg216, Glu242-Arg249, Glu145-Arg119 and Glu145-Arg152; while the most frequent interdomain interactions were: Glu35-Arg223 and Asp124-Arg223 (Fig. S20).

In addition, several hydrogen bonds were detected during the simulations (Tables S11 and S12). The Gln30-Ser215 hydrogen bond was established in all the trajectories and always with high persistence. Other frequently observed hydrogen bonds were: Thr254-Trp204 and Ser238-Arg216.

The matrix network interactions should be stabilised by three glutamine residues called glutamine brace. Of the three conserved glutamine brace residues, only Gln30 and Gln218 established hydrogen bonds with the matrix network residues. Indeed, when Gln30 interacted with Asp211 and Lys26, the distance between these two residues remained constant around 3 Å (Fig. 6). Similarly, when Gln121 interacted with Glu114 and Lys214, the interaction between those residues was stable (Figs. S21–S23). Conversely, the lack of interaction between the Gln braces and the matrix network residue pairs results in a destabilization of the charged couples salt bridges. This is the case for Gln121, Lys117 and Asp23, in all the simulations (Figs. S21–S23).

3.4. Arg160, Trp204 and Arg257 form a cation-π-cation interaction

During the MD simulations, the residue Trp204 contacted the guanidinium groups of Arg257 and Arg160. Analysis of distances and angles (Fig. 7C–F, Figs. S24–S26) strongly suggests the occurrence of cation-π interactions between the guanidinium group of Arg160 and the aromatic ring of Trp204, in a T-shaped manner, and between the guanidinium group of Arg257 and Trp204 aromatic ring, in a parallel manner (Fig. 7A, B) [44]. This pattern did not recur during MD1 of the SLC25A29-ARG complex, likely due to the different localization and interactions of the ligand (Fig. S25).

A similar behaviour was observed during the MD1 simulation with LYS, where the distances of the two arginine residues from Trp204 were below 6 Å, and the residues side chains relative orientations were parallel for Arg257 and orthogonal, for Arg160 (in particular between 50 and 175 ns) (Fig. 7). On the contrary, during MD3, the angle and distance between Arg160 and Trp204 side chains were less stable and incompatible with a cation-π interaction (Fig. S26).

Surprisingly, in the MD4 simulation, Arg257 and Arg160 established very strong interactions with Trp204, and both in a parallel manner. It is also interesting to note, that Arg160 was closer to Trp204 than Arg257 (Fig. S26).

The absence of ligands did not affect this network, as the distances and angles between Arg257, Arg160 and Trp204 during MD0 were very similar to those observed in the other MD simulations (Fig. S24).

3.5. Cardiolipin binding

Cardiolipin (CL) is known to have a functional role, interacting with the protein moiety of the ADP/ATP mitochondrial transporter [45]. For this reason, the SLC25A29 sequence motifs corresponding

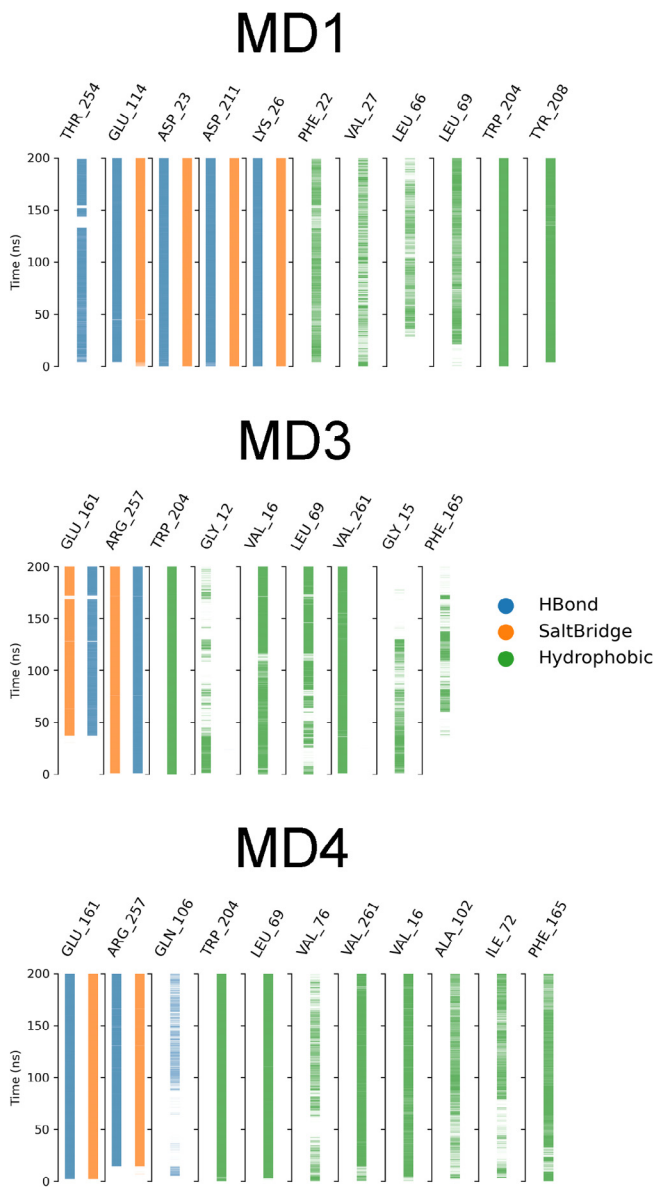

Fig. 3. Time series of the ARG-SLC25A29 interactions during the three MD simulations. The most significant interacting residues are shown; hydrogen bonds are depicted in blue, salt bridges in orange and hydrophobic interactions in green. (For interpretation of the references to color in this figure legend, the reader is referred to the web version of this article.)

to the cardiolipin binding sites in bANT1 [24,46,47] were identified from a sequence alignment (Fig. 1, Table S13) and used to analyse the interactions between CL molecules and SLC25A29 during the six MD simulations.

Notwithstanding the moderate amount of sampling (1.2 μs in total), it is worthwhile to note that three different binding sites were identified, which largely match the sequence motifs predicted from the alignment (Fig. 8, Table 4, Table S13). Binding site I resulted to be the most frequently occupied, with Ser64, Arg129 and Leu135 being the residues that mainly interacted with the CL headgroups (Fig. 8C, Table 4). In the case of binding site III, hydrogen bond interactions were observed with Thr42, Arg249 and Gly250 (Fig. 8E, Table 4). On the contrary, the binding of CL at site II was observed only during one of the MD simulations, where the CL headgroup interacted with Arg148 and Arg152 (Fig. 8D, Table 4).

Table 3
Analysis of water-mediated hydrogen bonds between the ARG/LYS ligands and protein residues (when possible, only the interactions with a persistence higher than 20% were reported).

SLC25A29 – ARG		SLC25A29 – LYS	
MD1		**MD1**	
Residues	**Fraction**	**Residues**	**Fraction**
ASP23 ARG	0.88	ASP23 LYS	0.35
ASP211 ARG	0.51		
THR254 ARG	0.35		
ASP211 SER215 ARG	0.22		
MD3		**MD3**	
Residues	**Fraction**	**Residues**	**Fraction**
ARG160 ARG	0.34	GLU114 LYS	0.11
GLU114 ARG	0.20		
MD4		**MD4**	
Residues	**Fraction**	**Residues**	**Fraction**
ASN73 ARG	0.41	ASP23 LYS	0.95
ARG160 ARG	0.35	GLU114 LYS	0.30
THR207 ARG	0.21	GLN106 LYS	0.23
SER203 ARG	0.20		

4. Discussion

The sequence similarity between SLC25A29 and bANT1 suggests structural similarity. This is confirmed by the fact that the homology model presented in this work has reliable statistics (Table S1). The choice of the 1OKC template for the modelling was somewhat an obligatory one. This could be a limitation giving the fact that this inhibited structure represents an abortive state of the transporter. However, MD simulations were carried out on purpose to relax the model structure and bring it into a more biologically relevant state.

The sequence alignment with bANT1, and the SLC25A29 structural model, predicted Gly68 (I), Arg160-Glu161(II) and Arg257 (III) to be the SLC25A29 CPs. According to the hypothesis for SLC25 ligand recognition, formulated by Robinson and Kunji [4], the first CP has the function to discriminate between different ligands of the same class (in this case, through the interaction with the side chain of the basic amino acid transported). Anyhow, given the apolar nature and the localization at the interface with H3, it is very unlikely that Gly68 is involved in such a task, as also suggested by MD simulations in which no contacts of this residue with the ligands were detected. However, the side chain carbonyl oxygen of a nearby residue, Asn73, is observed to interact through a bridging water molecule with the α-amino group of the ARG ligand (Fig. S19). Probably, a stronger interaction with the ligand could happen in an earlier recognition step, and this could also justify why it was not observed to interact with LYS. The role of Asn73 as CP I was also suggested in a previous review article [48], based on mutagenesis experiments of the human ornithine carrier 1 (ORC1), in which the mutation of the corresponding residue, Asn78, resulted in a reduction of the transporter activity [49]. On the other hand, during MD simulations with both ARG and LYS, CPs III (Arg257) recognized the carboxyl group of the ligands, exactly as suggested by the ligand recognition hypothesis, whereas

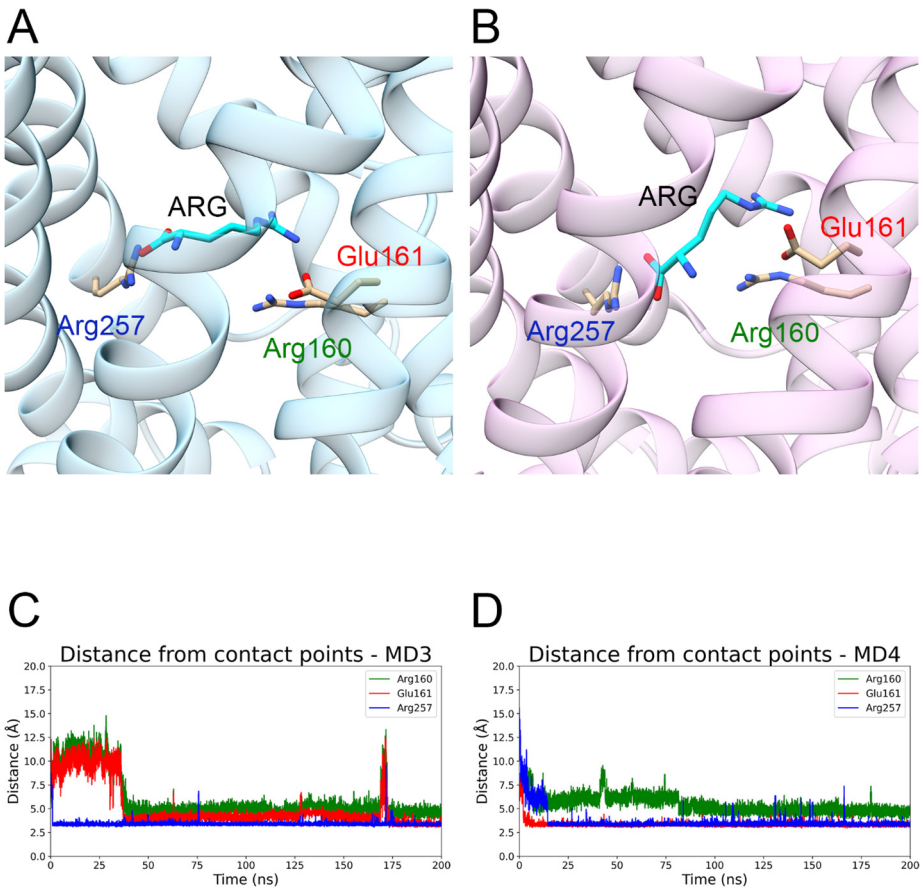

Fig. 4. ARG recognition during the third and fourth molecular dynamics simulations (MD3 and MD4). Top panels. Side view focus of the ARG-SLC25A29 complexes for MD3 (A) and MD4 (B) trajectories. ARG (blue) and contact points (tan) are depicted in sticks representation, while SLC25A29 structure is represented as blue (MD3) and pink (MD4) ribbons. Bottom panels. Plots of the ARG distance from contact points during MD3 (C) and MD4 (D) trajectories. (For interpretation of the references to color in this figure legend, the reader is referred to the web version of this article.)

Glu161 interacted with the guanidinium group and Arg160 with the α-amino group in an interaction mediated by a solvent molecule. Of course, given that the basic residues Arg160 and Arg257 tend to interact with the acidic moiety of the ligand, it is probable that the CP II residues (Arg160-Glu161) could interact with the α-amino and carboxyl group of the ligand in an earlier step of the transport process, and that Arg257 binding is responsible for the different orientation and stabilization of the transported ligand.

The starting ligand–protein complexes were obtained by docking simulations; however, few nanoseconds of MD simulations were sufficient to generate more stable binding modes or to exclude likely unrealistic complexes (*i.e.*, MD2 and MD5).

In this regard, in the MD simulations where the ARG was present, the changes in the ligand-CPs distances reflect the movement of the solute toward the binding residues, whereas the subtle differences are likely consequences of the two different protein conformations from which the two MD trajectories were started (Fig. 4, Tables 1, 2). Similarly, in the MD simulations where the LYS was present, the ligand interacted with the putative CP II and CP III, although establishing a higher number of less stable interactions during the trajectories (Fig. 5). In fact, LYS ligand explored much more space inside the cavity of the transporter with respect to ARG. Specifically, during MD1, while in the first half of the simulation the side chain amino and carboxyl groups of LYS interacted with Glu114 and Lys117, respectively, in the second half the ligand moved towards the central binding site with the side chain amino group interacting with Glu161, the carboxyl group with Arg257 and the α-amino group with Glu114. In a similar manner, during MD3, the carboxyl group and the α-amino group of LYS initially was bound to Lys26 and Glu114, while subsequently the movement of the ligand led to new interactions with Arg257 and Glu161. In the third trajectory, the binding mode was slightly more stable, the ligand establishing interactions with Lys117, Glu114 and Glu161.

Both the predicted SLC25A29 CP II and III are conserved in ORC1 (SLC25A15; 41.5% of sequence similarity with SLC25A29) and ORC2 (SLC25A2; 42.9% of sequence similarity with SLC25A29) [49], and in the mitochondrial carnitine/acylcarnitine carrier CAC (SLC25A20; 48.6% of sequence similarity with SLC25A29) [50,51]. It is worthwhile to note that mutations of the corresponding CP II residues in the bovine 2-oxoglutarate carrier (Arg190 and Ala191) resulted in a significant reduction of the transporter activity [52]. Moreover, site-directed mutagenesis and transport assays evidenced a critical role for residues Glu77, Asn78, Arg179, Glu180 and Arg275 in ORC1 (corresponding to SLC25A29 residues Ile72, Asn73, Arg160, Glu161 and Arg257) [49]. This evidence supports the proposed role for Asn73 as CP I and confirms that Arg160, Glu161 and Arg257 function as CP II and III, respectively, as demonstrated also by the activity decrease caused by the mutation of the corresponding residues Arg178, Asp179 and Arg275 in CAC [53]. Moreover, a study conducted on ORC1 by Monnè and colleagues [49] showed that the single mutation N74A did not affect the activity of the protein, while the N74Y mutation caused a significant decrease of the initial transport rate, probably due to a modification of the cavity shape. Noteworthy, the corresponding residue in SLC25A29 is Leu69, which is sterically equivalent to

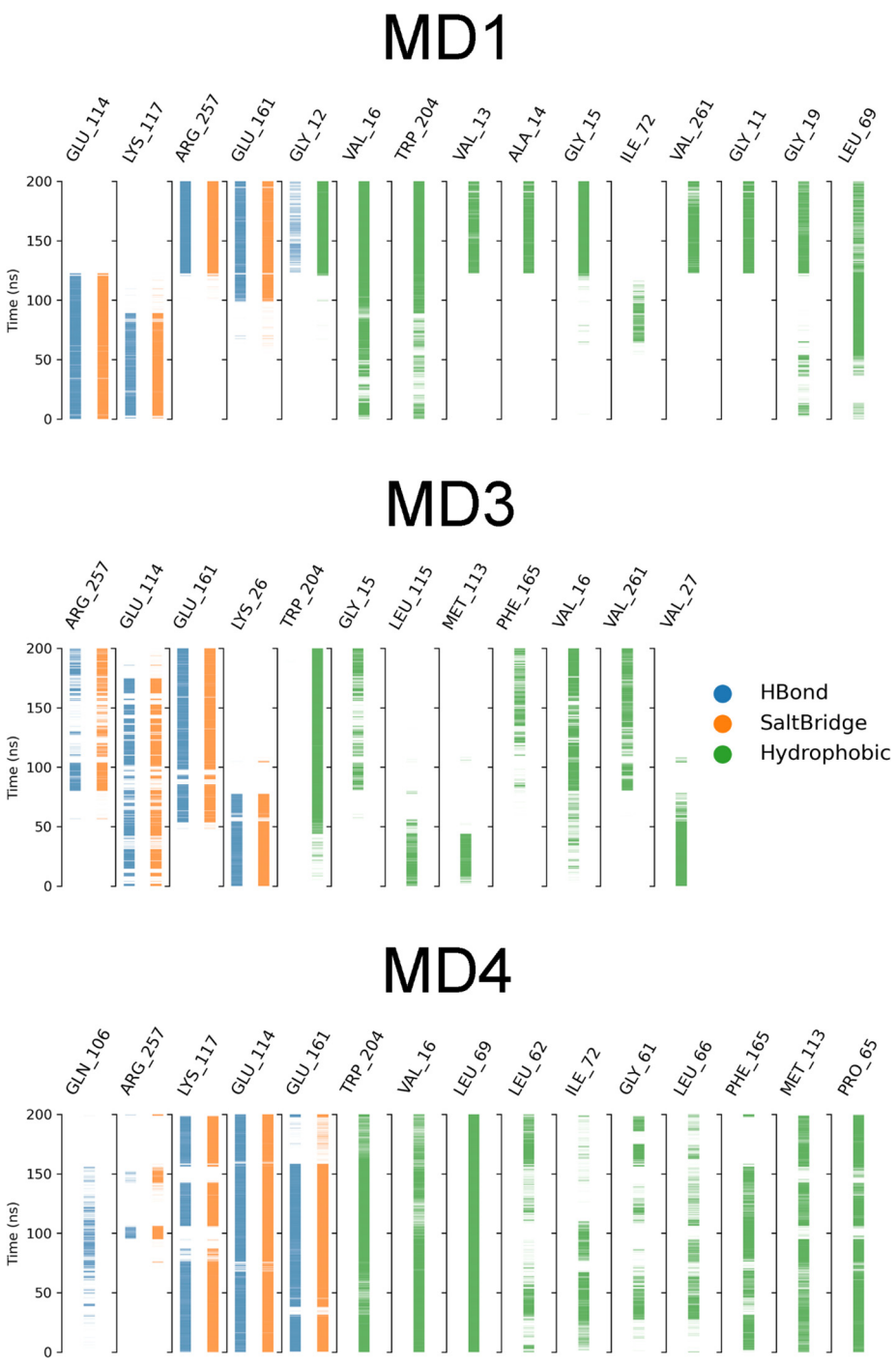

Fig. 5. Time series of the LYS-SLC25A29 interactions during the three MD simulations. The most significant interacting residues are shown; hydrogen bonds are depicted in blue, salt bridges in orange and hydrophobic interactions in green. (For interpretation of the references to color in this figure legend, the reader is referred to the web version of this article.)

Asn74 (Fig. S27) and thus it is likely to play a similar role in the transport mechanism. This is also supported by the MD simulations results, in which Leu69 was observed to establish hydrophobic contacts with both ARG and LYS ligands.

In addition, the same study proposed that Arg179 and Arg275 were connected through a cation-π interaction with Trp224, whose mutation also affected the activity and ligand specificity of the ORC1, ORC2 and CAC transporters [49,51]. Although classical MD force fields do not explicitly consider the π-electrons distribution, they, and in particular CHARMM36, can well reproduce cation-π interaction geometries [54]. Indeed, in almost all the six MD simulations, Trp204 (orthologue of ORC1, ORC2 and CAC Trp224) formed critical interactions with the ligand (hydrophobic contacts) and with Arg257 and Arg160 in what appears to be a cation-π-cation interaction (Fig. 7, Fig. S24–S26). This network result to be disrupted only during the first simulation with ARG (Fig. S24). Moreover, both Arg residues were in contact also with the ligand through electrostatic interactions. For this reason, as also observed in ORC1, ORC2 and CAC [49,51], this network could be needed to constrain Arg160 and Arg257 for ligand binding, while the move-

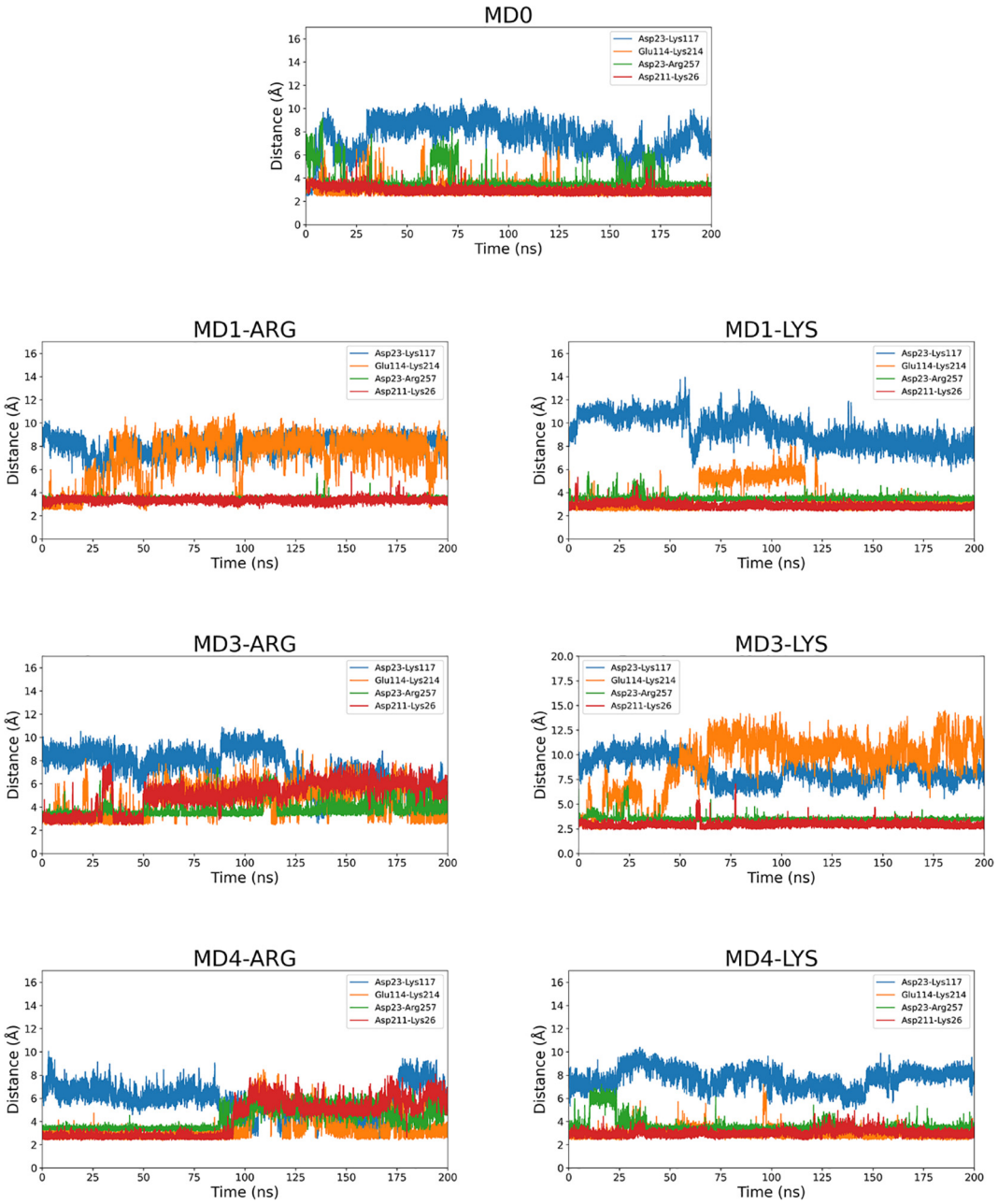

Fig. 6. Matrix network residues distances time series. The evolution over time of the distances between the side chains of the matrix network charged residues are here reported.

ment of these residues towards the matrix could cause the disruption of the matrix network and the release of the ligand. Indeed, the analysis of the intraprotein interactions highlighted a strong involvement of the above-mentioned basic residues in electrostatic interactions with the negatively charged matrix network residues. Regarding other interactions established by those residues, the salt bridges Asp23-Arg257 and Asp211-Arg160 were observed in almost all the simulations, with the former having on average a persistence next to 90%.

Indeed, the bANT1 Arg279 residue, corresponding to the SLC25A29 Arg257, was observed to establish electrostatic interactions with Glu29 (orthologue of SLC25A29 Asp23) during the binding of the ADP ligand or during long MD simulations [12,16]. Moreover, a different computational study, in which a bias perturbative force was applied to the matrix and cytoplasmic network residues, linked the Glu29-Arg279 salt bridge disruption to the asymmetric movement of H1, necessary for the matrix network opening [14]. In this regard, also the results presented in this study suggest that the first domain establishes only few interactions with the other domains, of which the Asp23-Arg257 salt bridge is probably the most important.

Of note, in addition to all the previously described interactions, the residue couples Lys26-Asp211 and Glu114-Lys214 established the canonical salt bridges involved in the matrix network formation, and mutation of the CAC residues corresponding to Lys26, Glu114, Asp211 and Lys214, resulted in a strong reduction of the transporter activity [50,53]. In contrast with the bANT1 crystallographic structures, the Asp23-Lys117 interaction was never observed, and this in line with other computational studies in which formation of this salt bridge is not observed [16]. This could

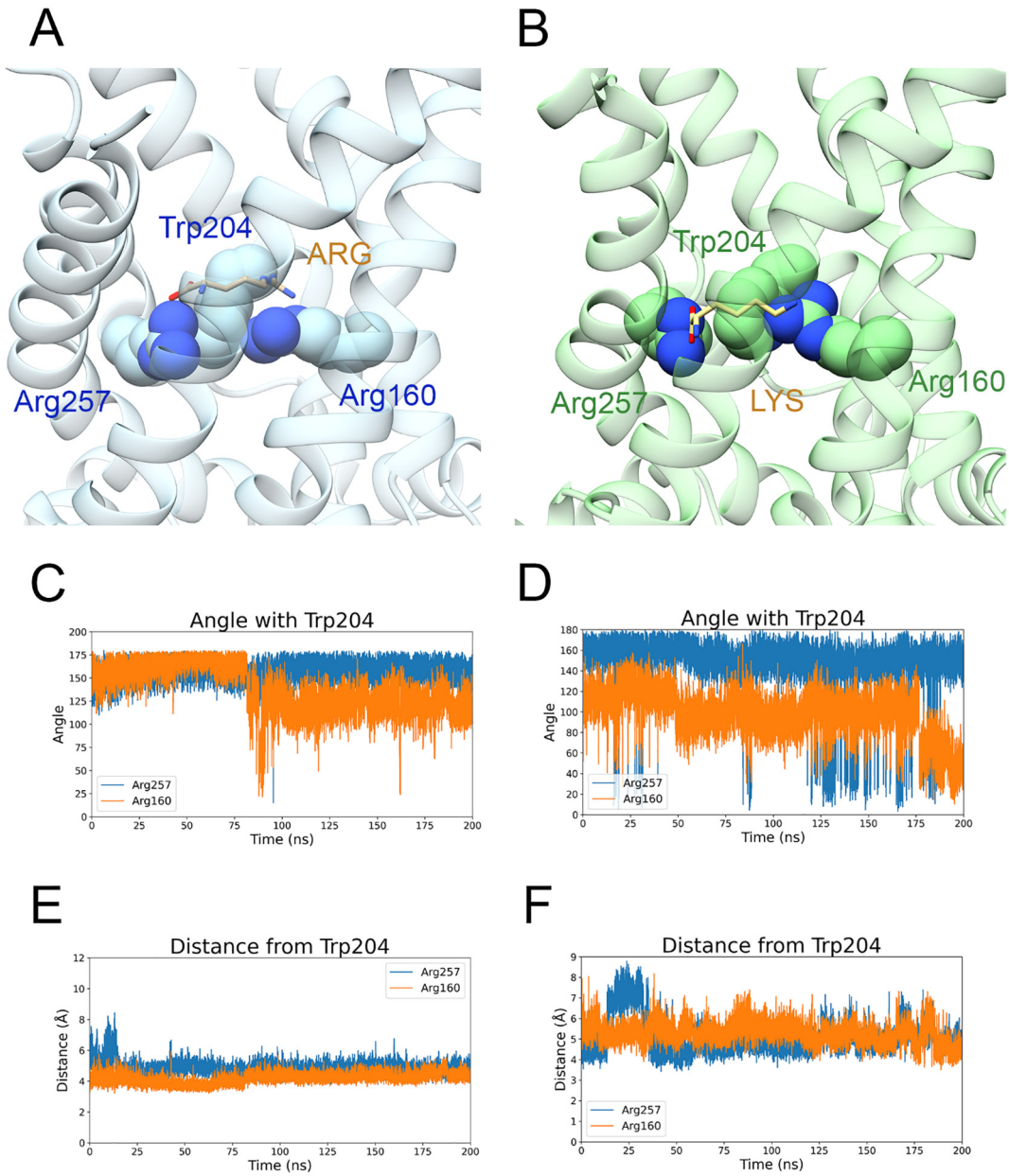

Fig. 7. Cation-π-cation interaction analysis. Top panels. Representative snapshots of the cation- π-cation interactions established between Arg257, Trp204 and Arg160, are illustrated for both MD4-ARG (A, blue) and MD1-LYS (B, green). The interacting residues are depicted as van der Waals spheres, while the protein backbone as ribbons. The ligands are depicted in stick representation and coloured in brown (ARG) and in light brown (LYS). Bottom panels. Angles and distances for MD4-ARG (C, E) and MD1-LYS (D, F) are plotted as a function of simulation time. In each graph, data relative to Arg257 and Arg160 are reported in blue and orange, respectively.

be due to the fact that the bANT1 crystal structure represents an inhibited, abortive state of the transporter, and indicates that MD simulations allowed to sample more biologically relevant conformations of the protein.

Indeed, in our simulations, Gln121 did not establish hydrogen bonds with these residues, as also no other interactions were observed to stabilize the interaction between domain 1 and 2, supporting the asymmetric interactions observed in other works on homologue transporters [16]. In this regard, the distances analyses between the matrix network residues clearly highlight the stabilization effect of the Gln braces hydrogen bonds over the Glu114-Lys214 and Asp211-Lys26 salt bridges. From these results, the Asp23-Arg257 salt bridge and the Ser215-Gln30 hydrogen bond turn out to be the most stable interactions among all the intraprotein interactions of the c-state.

In addition to the matrix network interactions, several other interactions have been identified, of which only few of them are interdomains ones. These analyses revealed that the three arginine residues Arg28, Arg119 and Arg216 were involved in interactions corresponding to those observed in the recent computational work published by the Cang group [16]. Specifically, significant interactions were established between Arg216 (bANT1 Arg236) and Glu242 (bANT1 Glu264), while Arg119 interacted with Glu145 (bANT1 Asp167). In contrast with bANT1, Arg28 (bANT1 Arg30) showed the weakest stabilizing effect.

During the first trajectory of the SLC25A29-ARG complex, the ligand was "trapped" inside the matrix network for all the simulation time. The ligand–protein interactions here established could mimic the interactions involved in the last steps of the transport process before the ligand release, which could involve the cation-

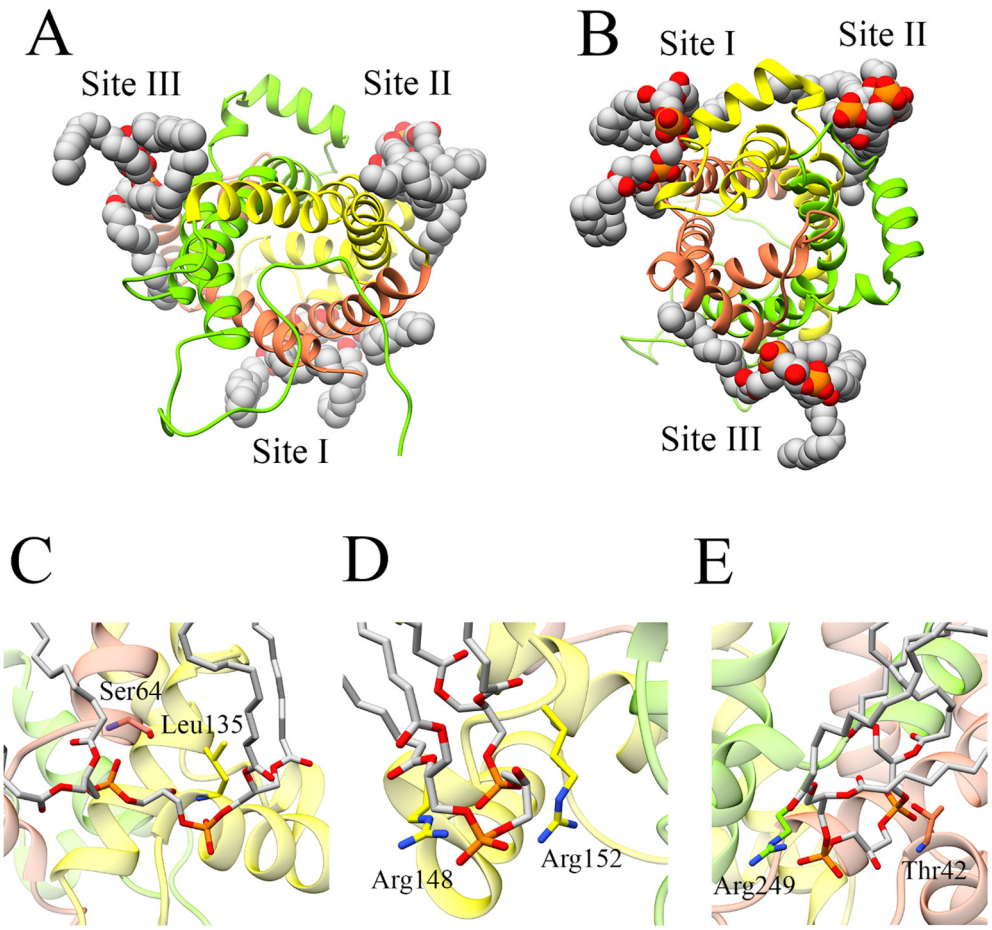

Fig. 8. Cardiolipin binding sites. Top panels. Representative snapshot of three cardiolipins (CL) (as spheres in grey) interacting with the SLC25A29 transporter (domain 1 in red, domain 2 in yellow, domain 3 in green). A) Top view; B) Bottom view. Bottom panels. Close up on the three main binding modes observed during the MD simulations. C) Binding site I; D) Binding site II; E) Binding site III. CL molecules (in grey) and interacting residues are shown as stick. Interacting residues are coloured according to the domain they belong. (For interpretation of the references to color in this figure legend, the reader is referred to the web version of this article.)

π-cation disruption, as well as the breaking of the Glu114-Lys214 and Arg160-Asp23 salt bridges.

Numerous efforts have been made to describe and explain the functional role of the CL lipids in the inner mitochondrial membrane, and in particular with respect to the SLC25 transporter mechanism [24,46,47]. From the analyses of the MD simulations here performed, several contacts have been observed between CL molecules and the SLC25A29 protein. Intriguingly, several of them are localized in the hypothetical binding sites corresponding to those identified for bANT1 (Fig. 8, Table 4, Table S13) [24,46,47]. This is particularly the case of the binding sites 1 and 3, where these lipid molecules mostly bind at the interface (Fig. 8, Table 4), while the interactions at site 2 are mainly intradomain. The presence of CLs in binding site 2 were observed to a smaller extent. This could be due to an insufficient amount of sampling or to an asymmetry in CL binding as also observed in other studies [46]. However, the spontaneous binding of randomly placed CLs further supports the goodness of the structural model and the reliability

Table 4
SLC25A29 residues involved in hydrogen bonds with cardiolipin molecules. The fraction was calculated dividing the number of frames where the interaction exists by the total 120,000 frames of the six trajectories considered.

SITE I		SITE II		SITE III	
Residue@atom	**Fraction**	**Residue@atom**	**Fraction**	**Residue@atom**	**Fraction**
SER64@OG	0.47	ARG152@NE	0.08	ARG249@NH1	0.23
SER64@N	0.30	ARG148@NE	0.07	GLY250@N	0.22
LEU135@N	0.23	ARG148@NH2	0.06	THR42@OG1	0.13
ARG129@NH2	0.24	ARG148@NH1	0.04	ALA252@N	0.08
ARG129@NH1	0.15			THR248@OG1	0.07
GLY61@N	0.10			ARG245@NH2	0.10
ASP136@N	0.06			THR42@N	0.10
ARG129@NE	0.04			ARG249@NH2	0.07
GLY63@N	0.04			LEU43@N	0.07
				ARG40@NH2	0.05
				GLY41@N	0.04

of the MD simulations, leading to identification of critical residues for the SLC25A29 correct functioning.

As a final consideration, it is interesting to note the presence of three vicinal Cys residues (*i.e.*, Cys107, Cys110 and Cys111) in the H3 helix of the SLC25A29 (Fig. S28). Evaluation of the different Cys side chain rotamers, through the backbone-dependent rotamer library [55] implemented in UCSF Chimera [41], evidences that the distances between the sulphur atoms are compatible with the formation of disulphide bonds. It is well known from the literature that vicinal Cys residues can be involved in redox-dependent regulation mechanisms and that NO can facilitate this event by S-nitrosylation of the thiol groups [56–58]. In this process, the presence of ionizable residues in the vicinity of the Cys residue, acting as either acids or bases, is critical for this reaction to occur [59]. In this regard, analysis of the structural model of SLC25A29 shows that several ionizable residues are in the proximity of the Cys residues cluster (Fig. S28). Taking into account the effect of SH reagents on the ORC1 transporter and the CAC regulation by S-nitrosylation [60,61], it is tempting to speculate that the vicinal Cys residues in SLC25A29 could act as a redox sensor. Interestingly, sequence alignment of SLC25A29 from vertebrates model organisms (*Homo sapiens*, *Podarcis muraiola, Gallus gallus*, *Xenopus laevis*, *Danio rerio*) reveals a strict conservation of all the three Cys residues (Fig. S29), suggesting that there is a selection pressure for conservation of these residues and thus a possible, biologically relevant, functional role.

5. Conclusions

The study here presented is the first attempt to computationally characterize the structure–function relationships of the SLC25A29 transporter. The high structural conservation of the SLC25 family members allowed to build a reliable model of this transporter and to analyse *in silico* the ligand recognition mechanism. The results of MD simulations in the presence of ARG and LYS ligands reinforce earlier predictions that Asn73, Arg160 and Glu161, and Arg257 represent the ligand contact points I, II, and III, respectively, providing an atomic-level view of the protein–ligand interactions. Moreover, the simulations highlight the stable character of the cation-π-cation interaction between Arg160, Trp204 and Arg257 and the relation with the ligand binding mode, suggesting that this interaction is critical for ligand binding and translocation. Further, spontaneous binding of cardiolipin molecules to the protein is observed at binding sites largely superimposable to those observed in the crystal structure of bANT1, lending support to the reliability of the model and MD simulations results. In conclusion, the results here presented could be useful to better explain the effect of pathogenic mutations, to guide experimental validation and possibly for future anti-cancer drugs development.

6. Data availability

Initial coordinates, molecular dynamics trajectories and representative snapshots have been deposited in the Zenodo repository (https://zenodo.org/record/4836274).

Funding

This research was funded by the Italian Ministry of University and Research (MIUR), grants "Dipartimenti di Eccellenza" (Legge 232/2016, Articolo 1, Comma 314–337) and PRIN (Grant No. 2017483NH8).

CRediT authorship contribution statement

Andrea Pasquadibisceglie: Conceptualization, Writing - original draft, Writing - review & editing. **Fabio Polticelli:** Investigation, Supervision, Project administration, Funding acquisition.

Declaration of Competing Interest

The authors declare that they have no known competing financial interests or personal relationships that could have appeared to influence the work reported in this paper.

Acknowledgments

Authors wish to thank Dr. Valentina Tortosa for helpful discussions.

Appendix A. Supplementary data

Supplementary data to this article can be found online at https://doi.org/10.1016/j.csbj.2021.10.007.

References

[1] Pebay-Peyroula E, Dahout-Gonzalez C, Kahn R, Trézéguet V, Lauquin G-M, Brandolin G. Structure of mitochondrial ADP/ATP carrier in complex with carboxyatractyloside. Nature 2003;426(6962):39–44. https://doi.org/10.1038/nature02056.

[2] Ruprecht JJ, King MS, Zögg T, Aleksandrova AA, Pardon E, Crichton PG, et al. The Molecular Mechanism of Transport by the Mitochondrial ADP/ATP Carrier. Cell 2019;176(3):435–447.e15. https://doi.org/10.1016/j.cell.2018.11.025.

[3] Ruprecht JJ, Kunji ER. Structural changes in the transport cycle of the mitochondrial ADP/ATP carrier. Curr Opin Struct Biol 2019;57:135–44. https://doi.org/10.1016/j.sbi.2019.03.029.

[4] Robinson AJ, Kunji ERS. Mitochondrial carriers in the cytoplasmic state have a common substrate binding site. Proc Natl Acad Sci U S A 2006;103(8):2617–22. https://doi.org/10.1073/pnas.0509994103.

[5] Robinson AJ, Overy C, Kunji ERS. The mechanism of transport by mitochondrial carriers based on analysis of symmetry. Proc Natl Acad Sci U S A 2008;105(46):17766–71. https://doi.org/10.1073/pnas.0809580105.

[6] Porcelli V, Fiermonte G, Longo A, Palmieri F. The human gene SLC25A29, of solute carrier family 25, encodes a mitochondrial transporter of basic amino acids. J Biol Chem 2014;289(19):13374–84. https://doi.org/10.1074/jbc.M114.547448.

[7] Sekoguchi Ei, Sato N, Yasui A, Fukada S, Nimura Y, Aburatani H, et al. A novel mitochondrial carnitine-acylcarnitine translocase induced by partial hepatectomy and fasting. J Biol Chem 2003;278(40):38796–802. https://doi.org/10.1074/jbc.M306372200.

[8] Camacho JA, Rioseco-Camacho N. The human and mouse SLC25A29 mitochondrial transporters rescue the deficient ornithine metabolism in fibroblasts of patients with the hyperornithinemia-hyperammonemia-homocitrullinuria (HHH) syndrome. Pediatr Res 2009;66(1):35–41. https://doi.org/10.1203/PDR.0b013e3181a283c1.

[9] Zhang H, Wang Q, Gu J, Yin Le, Liang S, Wu L, et al. Elevated mitochondrial SLC25A29 in cancer modulates metabolic status by increasing mitochondria-derived nitric oxide. Oncogene 2018;37(19):2545–58. https://doi.org/10.1038/s41388-018-0139-x.

[10] Zhou J, Wang X, Wang M, Chang Y, Zhang F, Ban Z, et al. The lysine catabolite saccharopine impairs development by disrupting mitochondrial homeostasis. J Cell Biol 2019;218:580–97. https://doi.org/10.1083/jcb.201807204.

[11] Dehez F, Pebay-Peyroula E, Chipot C. Binding of ADP in the mitochondrial ADP/ATP carrier is driven by an electrostatic funnel. J Am Chem Soc 2008;130(38):12725–33. https://doi.org/10.1021/ja8033087.

[12] Wang Y, Tajkhorshid E. Electrostatic funneling of substrate in mitochondrial inner membrane carriers. Proc Natl Acad Sci U S A 2008;105(28):9598–603. https://doi.org/10.1073/pnas.0801786105.

[13] Pietropaolo A, Pierri CL, Palmieri F, Klingenberg M. The switching mechanism of the mitochondrial ADP/ATP carrier explored by free-energy landscapes. Biochim Biophys Acta - Bioenerg 2016;1857(6):772–81. https://doi.org/10.1016/j.bbabio.2016.02.006.

[14] Tamura K, Hayashi S, Huang X. Atomistic modeling of alternating access of a mitochondrial ADP/ATP membrane transporter with molecular simulations. PLoS ONE 2017;12(7):e0181489. https://doi.org/10.1371/journal.pone.0181489.

[15] Falconi M, Chillemi G, Di Marino D, D'Annessa I, Morozzo della Rocca B, Palmieri L, et al. Structural dynamics of the mitochondrial ADP/ATP carrier revealed by molecular dynamics simulation studies. Proteins Struct Funct

Bioinforma 2006;65(3):681–91. https://doi.org/10.1002/prot.v65:310.1002/prot.21102.
[16] Yi Q, Li Q, Yao S, Chen Y, Guan MX, Cang X. Molecular dynamics simulations on apo ADP/ATP carrier shed new lights on the featured motif of the mitochondrial carriers. Mitochondrion 2019;47:94–102. https://doi.org/10.1016/j.mito.2019.05.006.
[17] Pasquadibisceglie A, Polticelli F. Computational studies of the mitochondrial carrier family SLC25. Present status and future perspectives. Bio-Algorithms and Med-Systems 2021;17(2):65–78. https://doi.org/10.1515/bams-2021-0018.
[18] Zimmermann L, Stephens A, Nam S-Z, Rau D, Kübler J, Lozajic M, et al. A Completely Reimplemented MPI Bioinformatics Toolkit with a New HHpred Server at its Core. J Mol Biol 2018;430(15):2237–43. https://doi.org/10.1016/j.jmb.2017.12.007.
[19] Mészáros B, Erdös G, Dosztányi Z. IUPred2A: Context-dependent prediction of protein disorder as a function of redox state and protein binding. Nucleic Acids Res 2018;46:W329–37. https://doi.org/10.1093/nar/gky384.
[20] Šali A, Blundell TL. Comparative protein modelling by satisfaction of spatial restraints. J Mol Biol 1993;234(3):779–815. https://doi.org/10.1006/jmbi.1993.1626.
[21] Williams CJ, Headd JJ, Moriarty NW, Prisant MG, Videau LL, Deis LN, et al. MolProbity: More and better reference data for improved all-atom structure validation. Protein Sci 2018;27(1):293–315. https://doi.org/10.1002/pro.3330.
[22] Smart OS, Neduvelil JG, Wang X, Wallace BA, Sansom MSP. HOLE: A program for the analysis of the pore dimensions of ion channel structural models. J Mol Graph 1996;14(6):354–60. https://doi.org/10.1016/S0263-7855(97)00009-X.
[23] Michaud-Agrawal N, Denning EJ, Woolf TB, Beckstein O. MDAnalysis: A toolkit for the analysis of molecular dynamics simulations. J Comput Chem 2011;32(10):2319–27. https://doi.org/10.1002/jcc.21787.
[24] Duncan AL, Ruprecht JJ, Kunji ERS, Robinson AJ. Cardiolipin dynamics and binding to conserved residues in the mitochondrial ADP/ATP carrier. Biochim Biophys Acta - Biomembr 2018;1860(5):1035–45. https://doi.org/10.1016/j.bbamem.2018.01.017.
[25] Daum G. Lipids of mitochondria. BBA - Rev Biomembr 1985;822(1):1–42. https://doi.org/10.1016/0304-4157(85)90002-4.
[26] Wu EL, Cheng Xi, Jo S, Rui H, Song KC, Dávila-Contreras EM, et al. CHARMM-GUI membrane builder toward realistic biological membrane simulations. J Comput Chem 2014;35(27):1997–2004. https://doi.org/10.1002/jcc.v35.2710.1002/jcc.23702.
[27] Huang J, Rauscher S, Nawrocki G, Ran T, Feig M, de Groot BL, et al. CHARMM36m: An improved force field for folded and intrinsically disordered proteins. Nat Methods 2017;14(1):71–3. https://doi.org/10.1038/nmeth.4067.
[28] Case DA, Ben-Shalom IY, Brozell SR, Cerutti DS, Cheatham III TE, Cruzeiro VWD, et al. AMBER 18. San Francisco: University of California; 2018.
[29] Darden T, York D, Pedersen L. Particle mesh Ewald: An N·log(N) method for Ewald sums in large systems. J Chem Phys 1993;98(12):10089–92. https://doi.org/10.1063/1.464397.
[30] Schneider T, Stoll E. Molecular-dynamics study of a three-dimensional one-component model for distortive phase transitions. Phys Rev B 1978;17(3):1302–22. https://doi.org/10.1103/PhysRevB.17.1302.
[31] Berendsen HJC, Postma JPM, van Gunsteren WF, DiNola A, Haak JR. Molecular dynamics with coupling to an external bath. J Chem Phys 1984;81(8):3684–90. https://doi.org/10.1063/1.448118.
[32] Ryckaert J-P, Ciccotti G, Berendsen HJC. Numerical integration of the Cartesian Equations of Motion of a System with Constraints: Molecular Dynamics of n-Alkanes. J Comput Phys 1977;23:321–41.
[33] Abraham MJ, Murtola T, Schulz R, Páll S, Smith JC, Hess B, et al. Gromacs: High performance molecular simulations through multi-level parallelism from laptops to supercomputers. SoftwareX 2015;1-2:19–25. https://doi.org/10.1016/j.softx.2015.06.001.
[34] Daura X, Gademann K, Jaun B, Seebach D, Van Gunsteren WF, Mark AE. Peptide folding: When simulation meets experiment. Angew Chemie - Int Ed 1999;38:236–40. https://doi.org/10.1002/(sici)1521-3773(19990115)38:1/2<236::aid-anie236>3.0.co;2-m.
[35] Morris GM, Huey R, Lindstrom W, Sanner MF, Belew RK, Goodsell DS, et al. Software news and updates AutoDock4 and AutoDockTools4: Automated docking with selective receptor flexibility. J Comput Chem 2009;30(16):2785–91. https://doi.org/10.1002/jcc.v30:1610.1002/jcc.21256.
[36] Trott O, Olson AJ. Software news and update AutoDock Vina: Improving the speed and accuracy of docking with a new scoring function, efficient optimization, and multithreading. J Comput Chem 2010;31:455–61. https://doi.org/10.1002/jcc.21334.
[37] Roe DR, Cheatham TE. PTRAJ and CPPTRAJ: Software for processing and analysis of molecular dynamics trajectory data. J Chem Theory Comput 2013;9(7):3084–95. https://doi.org/10.1021/ct400341p.
[38] Buchoux S. FATSLiM: a fast and robust software to analyze MD simulations of membranes. Bioinformatics 2017;33(1):133–4. https://doi.org/10.1093/bioinformatics/btw563.
[39] Hunter JD. Matplotlib: A 2D Graphics Environment. Comput Sci Eng 2007;9(3):90–5. https://doi.org/10.1109/MCSE.2007.55.
[40] McKinney W. Data Structures for Statistical Computing in Python. Proceedings of the 9th Python in Science Conference 2010:56–61. https://doi.org/10.25080/Majora-92bf1922-00a.
[41] Pettersen EF, Goddard TD, Huang CC, Couch GS, Greenblatt DM, Meng EC, et al. UCSF Chimera - A visualization system for exploratory research and analysis. J Comput Chem 2004;25(13):1605–12. https://doi.org/10.1002/jcc.v25:1310.1002/jcc.20084.
[42] Kunji ERS, Aleksandrova A, King MS, Majd H, Ashton VL, Cerson E, et al. The transport mechanism of the mitochondrial ADP/ATP carrier. Biochim Biophys Acta - Mol Cell Res 2016;1863(10):2379–93. https://doi.org/10.1016/j.bbamcr.2016.03.015.
[43] Waterhouse AM, Procter JB, Martin DMA, Clamp M, Barton GJ. Jalview Version 2–a multiple sequence alignment editor and analysis workbench. Bioinformatics 2009;25(9):1189–91. https://doi.org/10.1093/bioinformatics/btp033.
[44] Gallivan JP, Dougherty DA. Cation-π interactions in structural biology. Proc Natl Acad Sci U S A 1999;96:9459–64. https://doi.org/10.1073/pnas.96.17.9459.
[45] Klingenberg M. Cardiolipin and mitochondrial carriers. Biochim Biophys Acta - Biomembr 2009;1788(10):2048–58. https://doi.org/10.1016/j.bbamem.2009.06.007.
[46] Mao X, Yao S, Yi Q, Xu Z-M, Cang X. Function-related asymmetry of the specific cardiolipin binding sites on the mitochondrial ADP/ATP carrier. Biochim Biophys Acta - Biomembr 2021;1863(1):183466. https://doi.org/10.1016/j.bbamem.2020.183466.
[47] Hedger G, Rouse SL, Domański J, Chavent M, Koldsø H, Sansom MSP. Lipid-loving ANTs: molecular simulations of cardiolipin interactions and the organization of the adenine nucleotide translocase in model mitochondrial membranes. Biochemistry 2016;55(45):6238–49. https://doi.org/10.1021/acs.biochem.6b00751.
[48] Monné M, Miniero DV, Daddabbo L, Palmieri L, Porcelli V, Palmieri F. Mitochondrial transporters for ornithine and related amino acids: a review. Amin Acids 2015;47(9):1763–77. https://doi.org/10.1007/s00726-015-1990-5.
[49] Monné M, Miniero DV, Daddabbo L, Robinson AJ, Kunji ERS, Palmieri F. Substrate specificity of the two mitochondrial ornithine carriers can be swapped by single mutation in substrate binding site. J Biol Chem 2012;287(11):7925–34. https://doi.org/10.1074/jbc.M111.324855.
[50] Giangregorio N, Console L, Tonazzi A, Palmieri F, Indiveri C. Identification of amino acid residues underlying the antiport mechanism of the mitochondrial carnitine/acylcarnitine carrier by site-directed mutagenesis and chemical labeling. Biochemistry 2014;53(44):6924–33. https://doi.org/10.1021/bi5009112.
[51] Giangregorio N, Tonazzi A, Console L, Pistillo M, Scalera V, Indiveri C. Tryptophan 224 of the rat mitochondrial carnitine/acylcarnitine carrier is crucial for the antiport mechanism. Biochim Biophys Acta - Bioenerg 2019;1860(9):708–16. https://doi.org/10.1016/j.bbabio.2019.07.006.
[52] Stipani V, Cappello AR, Daddabbo L, Natuzzi D, Miniero DV, Stipani I, et al. The mitochondrial oxoglutarate carrier: Cysteine-scanning mutagenesis of transmembrane domain IV and sensitivity of Cys mutants to sulfhydryl reagents. Biochemistry 2001;40:15805–10. https://doi.org/10.1021/bi011616j.
[53] Giangregorio N, Tonazzi A, Console L, Indiveri C, Palmieri F. Site-directed mutagenesis of charged amino acids of the human mitochondrial carnitine/acylcarnitine carrier: Insight into the molecular mechanism of transport. Biochim Biophys Acta - Bioenerg 2010;1797(6-7):839–45. https://doi.org/10.1016/j.bbabio.2010.03.017.
[54] Minoux H, Chipot C. Cation-π interactions in proteins: Can simple models provide an accurate description? J Am Chem Soc 1999;121:10366–72. https://doi.org/10.1021/ja990914p.
[55] Shapovalov M, Dunbrack R. A smoothed backbone-dependent rotamer library for proteins derived from adaptive kernel density estimates and regressions. Structure 2011;19(6):844–58. https://doi.org/10.1016/j.str.2011.03.019.
[56] Caselli A, Camici G, Manao G, Moneti G, Pazzagli L, Cappugi G, et al. Nitric oxide causes inactivation of the low molecular weight phosphotyrosine protein phosphatase. J Biol Chem 1994;269(40):24878–82. https://doi.org/10.1016/S0021-9258(17)31472-2.
[57] Chiarugi P, Fiaschi T, Taddei ML, Talini D, Giannoni E, Raugei G, et al. Two vicinal cysteines confer a peculiar redox regulation to low molecular weight protein tyrosine phosphatase in response to platelet-derived growth factor receptor stimulation. J Biol Chem 2001;276(36):33478–87. https://doi.org/10.1074/jbc.M102302200.
[58] Wong PSY, Hyun J, Fukuto JM, Shirota FN, DeMaster EG, Shoeman DW, et al. Reaction between S-Nitrosothiols and thiols: Generation of nitroxyl (HNO) and subsequent chemistry. Biochemistry 1998;37:5362–71. https://doi.org/10.1021/bi973153g.
[59] Ascenzi P, Colasanti M, Persichini T, Muolo M, Polticelli F, Venturini G, et al. Re-evaluation of amino acid sequence and structural consensus rules for cysteine-nitric oxide reactivity. Biol Chem 2000;381:623–7. https://doi.org/10.1515/BC.2000.081.
[60] Giangregorio N, Tonazzi A, Console L, Galluccio M, Porcelli V, Indiveri C. Structure/function relationships of the human mitochondrial ornithine/citrulline carrier by Cys site-directed mutagenesis. Relevance to mercury toxicity. Int J Biol Macromol 2018;120:93–9. https://doi.org/10.1016/j.ijbiomac.2018.08.069.
[61] Tonazzi A, Giangregorio N, Console L, De Palma A, Indiveri C. Nitric oxide inhibits the mitochondrial carnitine/acylcarnitine carrier through reversible S-nitrosylation of cysteine 136. Biochim Biophys Acta - Bioenerg 2017;1858(7):475–82. https://doi.org/10.1016/j.bbabio.2017.04.002.